Journal of Materials Chemistry A

ROYAL SOCIETY OF CHEMISTRY

PAPER

Published on 27 August 2026
Licence and permissions

Check for updates

Cite this: J. Mater. Chem. A, 2026, 14, 39367

Interfacial polarization triggered by low-*k* fillers boosts piezoelectricity of MMT/PT composites for intelligent health monitoring

Yong Ao,[a] Junjun Yuan,[a] Wenqi Yu,[a] Rui Yuan,[b] Boling Lan,[a] Shenglong Wang,[a] Tingting Zhou,[a] Guicen Liu,[a] Wei Zhao,[a] Zhiyuan Gao,[a] Xiaofei Jiang,[a] Weili Deng,[a] Long Jin*[a] and Weiqing Yang *[ac]

Poly(vinylidene fluoride-trifluoroethylene) (P(VDF-TrFE), PT) is a promising piezoelectric polymer for flexible electronics, but its output remains insufficient for reliable health monitoring of subtle motions and vital signs. Conventional strategies employ high-permittivity (high-*k*) nanofillers to enhance piezoelectricity *via* interfacial polarization, yet they inevitably increase leakage current and obscure the genuine contribution of interface effects. Here, we challenge this paradigm by incorporating low-permittivity (low-*k*) montmorillonite (MMT) nanosheets into PT. Despite theoretical expectations of reduced permittivity, the large-aspect-ratio MMT creates extensive interfacial regions where permittivity mismatch induces localized polarization, promoting a *gauche* to all-*trans* conformational transition in polymer chains as verified by theoretical calculations and experimental characterization. Electromechanical measurements reveal a concentration-dependent enhancement peaking at 4 wt% MMT, achieving an eight-fold increase in voltage and three-fold increase in current compared to pristine PT. The optimized composite is fabricated into flexible sensors that clearly resolve distinct patterns of walking, jumping, squatting, and shoulder asymmetry. This work resolves the apparent paradox between theoretical prediction and experimental performance, establishing low-*k* two-dimensional materials as a viable and versatile platform for interfacial polarization engineering in high-performance flexible piezoelectric composites.

Received 14th July 2026
Accepted 24th August 2026

DOI: 10.1039/d6ta05902c

rsc.li/materials-a

Introduction

Advanced materials for electromechanical conversion are central to the advancement of consumer electronics, flexible wearable devices, and intelligent sensors.[1] Piezoelectric materials, as intrinsically electromechanically active materials, offer high reliability and superior durability.[2] Among them, poly(-vinylidene fluoride-trifluoroethylene) (P(VDF-TrFE), PT) stands out due to its excellent piezoelectric properties, lightweight flexibility, and biocompatibility.[3,4] Yet its piezoelectric output, while promising, falls short of the amplitude required for reliable health monitoring of subtle joint motions and vital signs, leaving weak signals indistinguishable from environmental noise.[5–8]

While chemical approaches (*e.g.*, TrFE ratio tuning to mimic a morphotropic phase boundary) can boost intrinsic activity, physical blending is more practical and economically viable.[9,10] Particularly when coupled with electrospinning, physical blending is able to simultaneously induce electric field polarization and mechanical stretching to promote piezoelectric phase formation.[11–13] The incorporation of nanofillers into this framework has attracted growing interest,[14–17] not merely for mechanical reinforcement, but because recent studies have revealed that even non-piezoelectric fillers can enhance the overall piezoelectric response, which is a counterintuitive effect primarily attributed to interfacial polarization.[18,19] Interfacial polarization arises from the surface polarity of the filler and the interfacial interactions with the matrix molecular chains. The polarity induction drives conformational changes in the matrix chains, promoting the formation and stabilization of polar conformations. Two-dimensional (2D) materials—such as MXene, graphene, and black phosphorus—are especially attractive in this context, offering extensive interfacial area, mechanical flexibility, and surface tunability.[20–26] Consequently, interfacial polarization engineering has become a prominent strategy for enhancing polymer piezoelectricity.[27–30] However, nearly all such composites rely on high-permittivity (high-*k*)

[a]*Key Laboratory of Advanced Technologies of Materials, Ministry of Education, School of Materials Science and Engineering, Southwest Jiaotong University, Chengdu, 610031, China. E-mail: longjin@swjtu.edu.cn; wqyang@swjtu.edu.cn*

[b]*School of Physical Science and Technology, Southwest Jiaotong University, Chengdu 610031, China*

[c]*Research Institute of Frontier Science, Southwest Jiaotong University, Chengdu 610031, China*

fillers to amplify interfacial polarization,[31] following the conventional wisdom that piezoelectric coefficient scales with permittivity ($d_{33} \propto \varepsilon_r$).[32,33] This dependence creates a critical dilemma: high-*k* fillers inevitably raise the risk of increasing leakage current,[34] which hinders efficient poling of the composite and obscures the genuine contribution of interfacial polarization to piezoelectricity.[35–37] In contrast, low-permittivity (low-*k*) fillers would eliminate leakage concerns and allow the effect of interfacial polarization to be directly demonstrated. Yet in theory they decrease the composite's overall permittivity, would appear to diminish rather than enhance piezoelectricity. This apparent contradiction has left the low-*k* pathway largely unexplored.

Herein, enhanced piezoelectric performance in PT is achieved through the incorporation of low-permittivity (low-*k*) montmorillonite (MMT) nanosheets, challenging the conventional reliance on high-*k* fillers. The large-aspect-ratio MMT creates extensive interfacial regions where permittivity mismatch generates localized polarization. This interfacial effect promotes a *gauche* to all-*trans* conformational transition in the polymer chains, as corroborated by theoretical calculations and experimental characterization. Electromechanical measurement reveals a concentration-dependent output that peaks at 4 wt% MMT, an eight-fold voltage and three-fold current enhancement. Finally, the optimized MMT/PT composite is fabricated into flexible sensors that resolve distinct patterns of walking, jumping, squatting, and shoulder asymmetry. These findings resolve the apparent paradox between theoretical prediction and experimental potential, establishing interfacial polarization engineering with low-*k* 2D materials as a viable and versatile strategy for advancing flexible piezoelectric composites.

Results and discussion

Conceptions and design of MMT/PT piezoelectric composite for sensing

Wearable electronics require precise movement and force application, where the piezoelectric sensor is an ideal candidate for advanced activities monitoring. MMT/PT piezoelectric composite mats were fabricated *via* electrospinning for electromechanical conversion and pressure sensing applications (Fig. 1a). In contrast to conventional high-*k* nanomaterial-based approaches, interfacial polarization was triggered herein by incorporating low-*k* MMT nanosheets (Fig. S1). This strategy simultaneously promotes the *gauche* to all-*trans* conformational transition in PT molecular chains through interfacial polarization (Fig. 1b) while suppressing the high leakage current associated with high-*k* fillers. The morphology and elemental distribution of the as-prepared mats were characterized by scanning electron microscopy (SEM) and energy-dispersive X-ray spectroscopy (EDS) (Fig. S2). The electrospun MMT/PT fibers exhibited uniform, bead-free morphologies with characteristic nanoscale features conducive to enhanced electromechanical conversion (Fig. S3). The EDS mapping confirmed the homogeneous distribution of MMT nanosheets throughout the polymer matrix, with elemental signals corresponding to Al and Si from MMT colocalized with C and F from PT. This uniform dispersion is essential for generating consistent interfacial polarization across the composite. The freestanding mat exhibited macroscopic flexibility and mechanical integrity, as shown in the digital photograph (Fig. 1c), withstanding various deformations including bending, twisting, and stretching without structural failure. To assess practical utility, MMT/PT sensors were mounted on the human plantar surface for monitoring pressure signals, enabling clear discrimination of distinct motion patterns (Fig. 1d). Extending this application to healthcare, the sensor successfully distinguished between normal posture and shoulder asymmetry—a common postural deviation with health implications—based on significant differences in plantar pressure signals (Fig. 1e), highlighting its promise for intelligent medical sensing.

Characterization of interfacial polarized MMT/PT piezoelectric composite

To elucidate the origin of interfacial polarization in MMT/PT composites and its subsequent effects on the polymer matrix, a combined computational and experimental approach was employed. Density functional theory (DFT) simulations first probed the potential interactions between MMT nanosheets and PT molecular chains. The results revealed that the interaction between PT and MMT is limited to weak van der Waals forces, with no evidence of bond formation or strong interactions such as hydrogen bonding (Fig. 2a). This absence of significant electronic coupling or charge transfer indicates that interfacial polarization in this system cannot originate from chemical interactions at the filler-matrix interface. An alternative mechanism for interfacial polarization arises from permittivity mismatch between composite components. In MMT/PT, the incorporated MMT nanosheets possess a lower relative permittivity than the PT matrix. Under an applied electric field, this permittivity contrast induces spatial heterogeneity in the local field distribution, particularly in the interfacial regions adjacent to the MMT nanosheets. Finite element simulation confirmed this hypothesis: under an external bias, a pronounced difference in electric field intensity was observed between the MMT domains and the surrounding PT matrix (Fig. 2b). This field discontinuity at the interfaces generates localized polarization, establishing permittivity mismatch as the physical origin of interfacial polarization in MMT/PT composites. The DFT and simulation findings were corroborated by X-ray photoelectron spectroscopy (XPS). As shown in Fig. 2c, MMT nanosheets exhibited characteristic core-level spectra—Si, Al, and O—with no detectable chemical shifts or additional bonding states (Fig. S4). The absence of spectral perturbations confirms that the MMT surface lacks readily available binding sites for strong interactions with PT, reinforcing the conclusion that interfacial polarization arises from permittivity mismatch rather than chemical coupling.

With the polarization mechanism established, attention turned to its influence on the PT matrix—first at the crystallographic level, then at the molecular level. X-ray diffraction (XRD) patterns of pristine PT and MMT/PT were strikingly

 This journal is © The Royal Society of Chemistry 2026

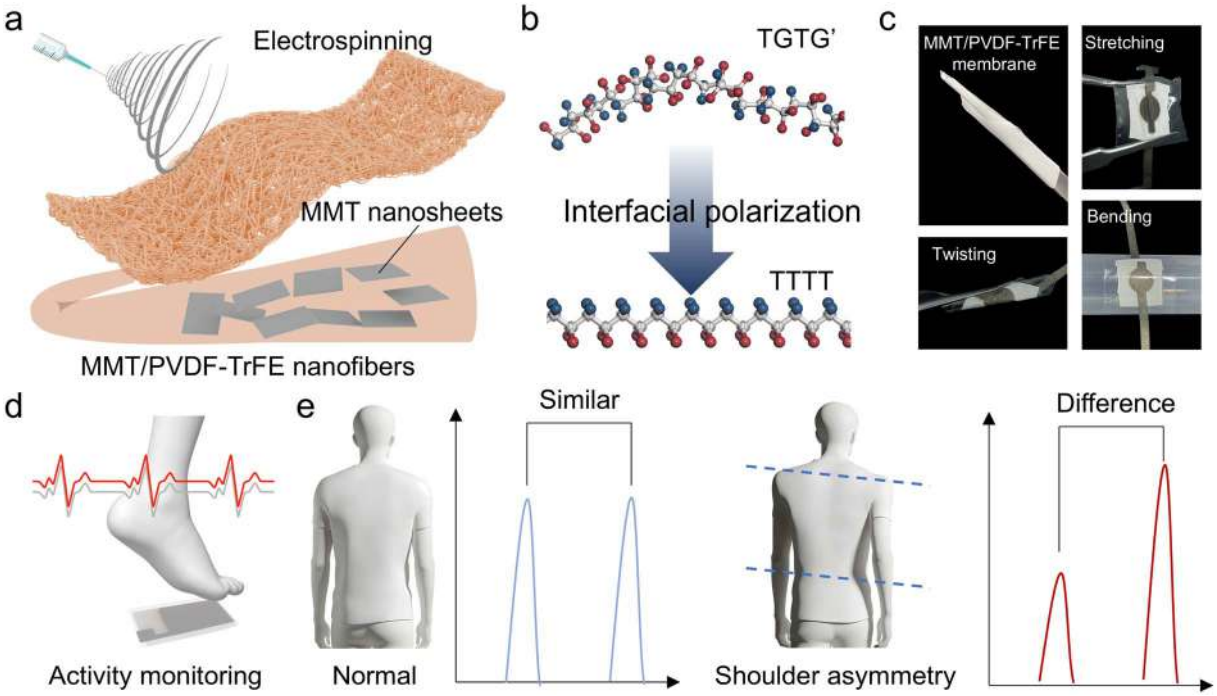


Fig. 1 Conceptions and design of MMT/PT piezoelectric composite for activity recognizing. (a) Schematic illustration of preparing MMT/PT piezoelectric mat *via* electrospinning. (b) Schematic illustration of molecular conformation transforms through interfacial polarization. (c) Photographic images presenting mechanical compliance of piezoelectric sensors. (d) Schematic illustration of activity monitoring through plantar piezoelectric sensing. (e) Schematic illustration of diagnosing shoulder asymmetry through piezoelectric sensing.

similar (Fig. 2d). Both exhibited the characteristic (110/200) reflection of the ferroelectric β-phase at $2\theta \approx 20.0°$, with nearly identical peak positions and widths. This morphological congruence demonstrates that MMT incorporation does not alter crystal phase or crystallite size—a finding reinforced by differential scanning calorimetry (DSC). The Curie and crystallization temperatures of the composite closely mirrored those of the pristine polymer (Fig. 2e), with only a marginal increase in crystallinity attributable to the nucleation effect of MMT nanosheets (Fig. 2f). These modest crystallographic differences cannot account for the substantial enhancement in piezoelectric performance, pointing toward a more fundamental mechanism operating at the molecular scale. Fourier-transform infrared (FTIR) spectroscopy revealed the molecular-level transformation. While the overall spectral features of pristine PT and MMT/PT were similar, distinct differences emerged at conformation-sensitive absorption bands (Fig. 2g). The composite exhibited diminished intensity at 840 cm^{-1} (characteristic of the *gauche* conformation) and enhanced intensity at 1279 cm^{-1} (characteristic of the all-*trans* conformation) (Fig. 2h). This spectral evolution indicates that interfacial polarization, arising from permittivity mismatch at the MMT-polymer interfaces, actively biases the polymer chains toward the all-*trans* conformation. Raman spectroscopy provided independent corroboration. The intensity ratio of the 1279 cm^{-1} band to the 840 cm^{-1} band (I_{1279}/I_{840}) serves as a semi-quantitative indicator of relative all-*trans* content. As shown in Fig. 2i, this ratio was notably higher for MMT/PT compared to pristine PT—a trend consistent across both spectroscopic techniques. The convergence of FTIR and Raman evidence demonstrates that interfacial polarization promotes the *gauche* to all-*trans* conformational transition. These results establish that MMT nanosheets enhance piezoelectric performance through interfacial polarization-driven conformational regulation.

Characterization of MMT/PT piezoelectric sensor

To evaluate the influence of interfacial polarization on the macroscopic piezoelectric response, MMT/PT composites were fabricated into piezoelectric sensors using a conventional sandwich structure, schematically illustrated in the exploded-view diagram (Fig. 3a and S6). Electromechanical characterization was performed on a custom-built testing platform to ensure accurate and reliable measurement of the sensor output (Fig. S7).

Interfacial polarization arises primarily at the interfaces between MMT nanosheets and the PT matrix; its magnitude is therefore intrinsically linked to the total interfacial area within the composite. Given the 2D morphology of MMT, the interfacial content is predominantly governed by the MMT loading concentration. To establish this correlation, a series of composites with varying MMT concentrations was fabricated, and their electrical output was systematically characterized. Fig. 3b, c and S8 present the output voltage and current of sensors with different MMT loadings. A monotonic increase in piezoelectric output was observed with increasing MMT

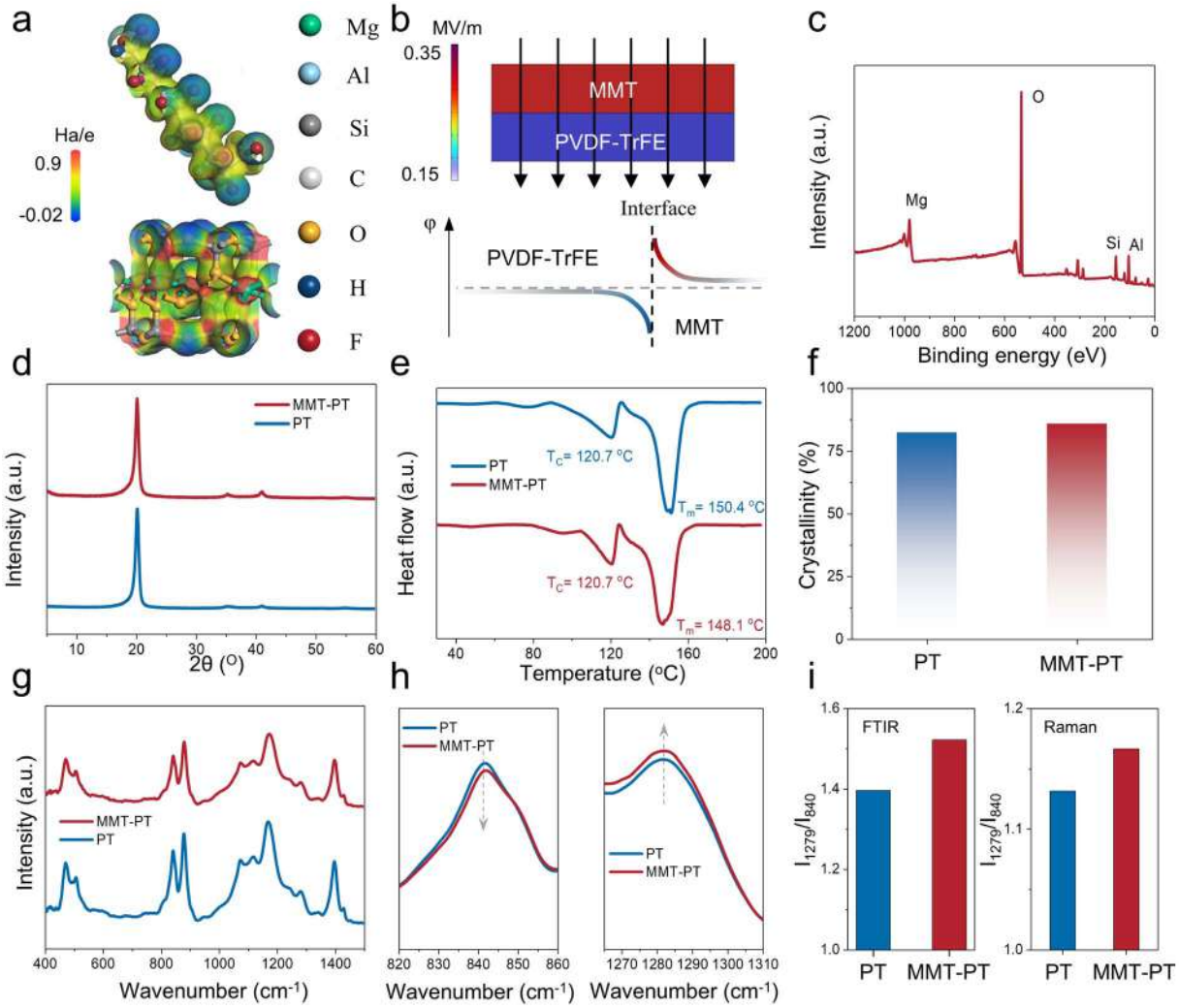


Fig. 2 Characterization of MMT/PT piezoelectric composite. (a) DFT calculations of PVDF-TrFE chain on the surface of MMT nanosheets. (b) Schematic illustration of permittivity mismatch inducing interfacial polarization. (c) XPS of MMT nanosheets. (d) XRD patterns of MMT/PT and PT. (e) DSC thermogram of MMT-PT and PT. (f) Crystallinity of MMT/PT and PT calculated from (e). (g) FTIR spectra of MMT/PT and PT. (h) Local comparison of FTIR for MMT/PT and PT. (i) Comparison of characteristic peak intensities between TTTT and TGTG′ for MMT/PT and PT.

content, reaching a maximum at 4 wt%—with an output voltage approaching 4 V, representing an approximately eight-fold enhancement compared to the 1 wt% composite, while the output current exhibited a more than three-fold increase. In addition, the output power density of the sensor was calculated and compared with that of previously reported piezoelectric sensors (Table S1). This concentration-dependent enhancement corroborates the pivotal role of interfacial polarization in boosting the piezoelectric response.

However, a sharp decline in output was observed when the MMT content reached 5 wt%. Such behavior is not rare in composite systems and is indicative of a percolation phenomenon:[9,10,38] when the filler concentration exceeds a critical threshold—the percolation threshold—a dramatic transition in material properties occurs (Fig. 3d). To investigate this phenomenon, finite element simulations of dielectric breakdown were performed on model systems representing MMT/PT and pristine PT (Fig. 3e). Comparative analysis of the simulated current paths revealed that at excessive MMT loadings (above the percolation threshold), the formation of connected filler networks facilitates current propagation through the material, increasing the susceptibility to dielectric breakdown and irreversible phase damage (Fig. S9). These results suggest that beyond the optimal concentration, interconnected MMT nanosheets provide pathways for charge transport and recombination, leading to attenuation of the overall piezoelectric performance.

Based on these findings, the composite with 4 wt% MMT was selected for subsequent sensor fabrication and application studies. As shown in Fig. 3f, the sensor exhibited a linear electromechanical response characteristic of piezoelectric devices, with excellent response characteristics—a response time of 30 ms and a recovery time of 60 ms (Fig. 3g). Furthermore, the sensor demonstrated operational stability, maintaining its initial output and response characteristics after more than 5000 consecutive operating cycles (Fig. 3h, i and S10). The results

 This journal is © The Royal Society of Chemistry 2026

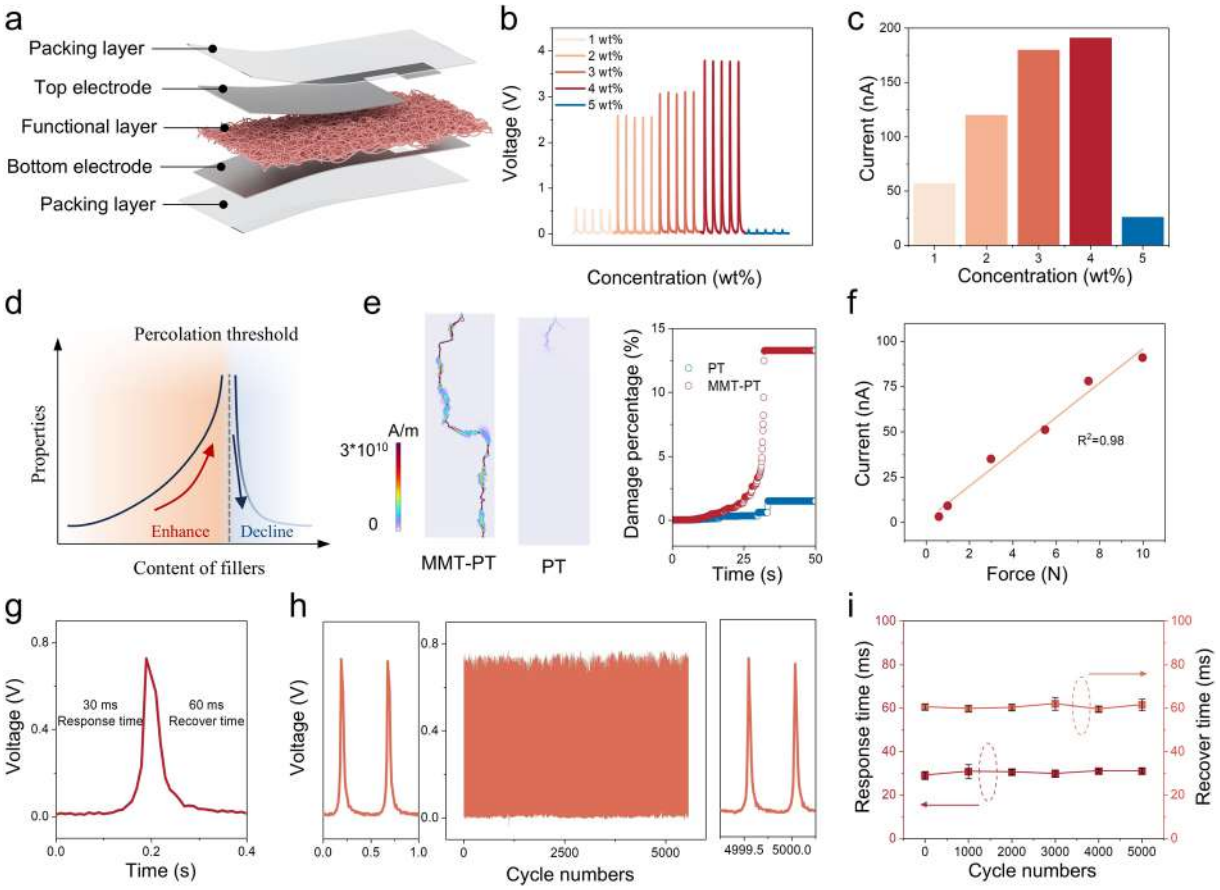


Fig. 3 Electrical characterization and mechanism of MMT/PT piezoelectric sensor. (a) Schematic illustration of piezoelectric sensor in explosive view. (b) Output voltage and (c) corresponding current of the sensors as a function of MMT concentration. (d) Schematical illustration of the percolation effect and its impact on piezoelectric properties. (e) Simulated dielectric breakdown current paths in MMT/PT *versus* PT (left); and corresponding fraction of damaged tissue as a function of time (right). (f) Electric output of sensor as a function of force. (g) Response and recover time of piezoelectric sensor. (h) Durability test results of sensor. (i) Evolution of sensor's response and recover time during durability testing.

demonstrate that the sensor retains its output signal amplitude without attenuation (Fig. 3h) and maintains a comparable response speed (Fig. 3i) to external mechanical stimuli even after 5000 cycles. This robust performance establishes a solid foundation for subsequent signal monitoring and recognition applications.

Plantar signal monitoring for exploring potential applications

The rapid advancement of embodied intelligence and intelligent healthcare has driven substantial interest in flexible, wearable smart sensors. Leveraging the favorable electromechanical performance of the MMT/PT composite, its potential for practical applications was further explored. Human physiological characteristics—including body weight, postural asymmetry, and injury—are often reflected in alterations of daily motor activities. Hence, the monitoring and recognition of such activities constitute a critical function for wearable sensors. The fibrous architecture of the electrospun MMT/PT mat imparts fabric-like properties, including favorable moisture permeability and stretchability (Fig. S11 and S12), rendering it well-suited for skin-attachable applications.

Based on these attributes, the sensor was attached to the plantar surface to monitor and acquire electrical signals generated during three typical daily activities: walking, running, and jumping (Fig. 4a–c). Distinct signal patterns were observed for each activity, characterized by unique amplitude, frequency, and temporal profiles. To enable automatic classification, a deep learning algorithm was constructed to learn and discriminate the signal features associated with the three activities (Fig. 4d). As shown in Fig. 4e and f, the model exhibited excellent accuracy and robustness in signal classification, achieving an overall recognition accuracy of 96.7%. These results confirm that the MMT/PT sensor fulfills the essential requirements for flexible wearable devices and holds considerable promise for practical deployment. Building on this foundation, the sensor was further applied to the detection of shoulder asymmetry—a common postural abnormality—to preliminarily explore its potential in intelligent healthcare. Individuals with shoulder asymmetry are at increased long-term risk for chronic and neurological disorders. This postural deviation often leads to uneven load distribution between the left and right feet during locomotion

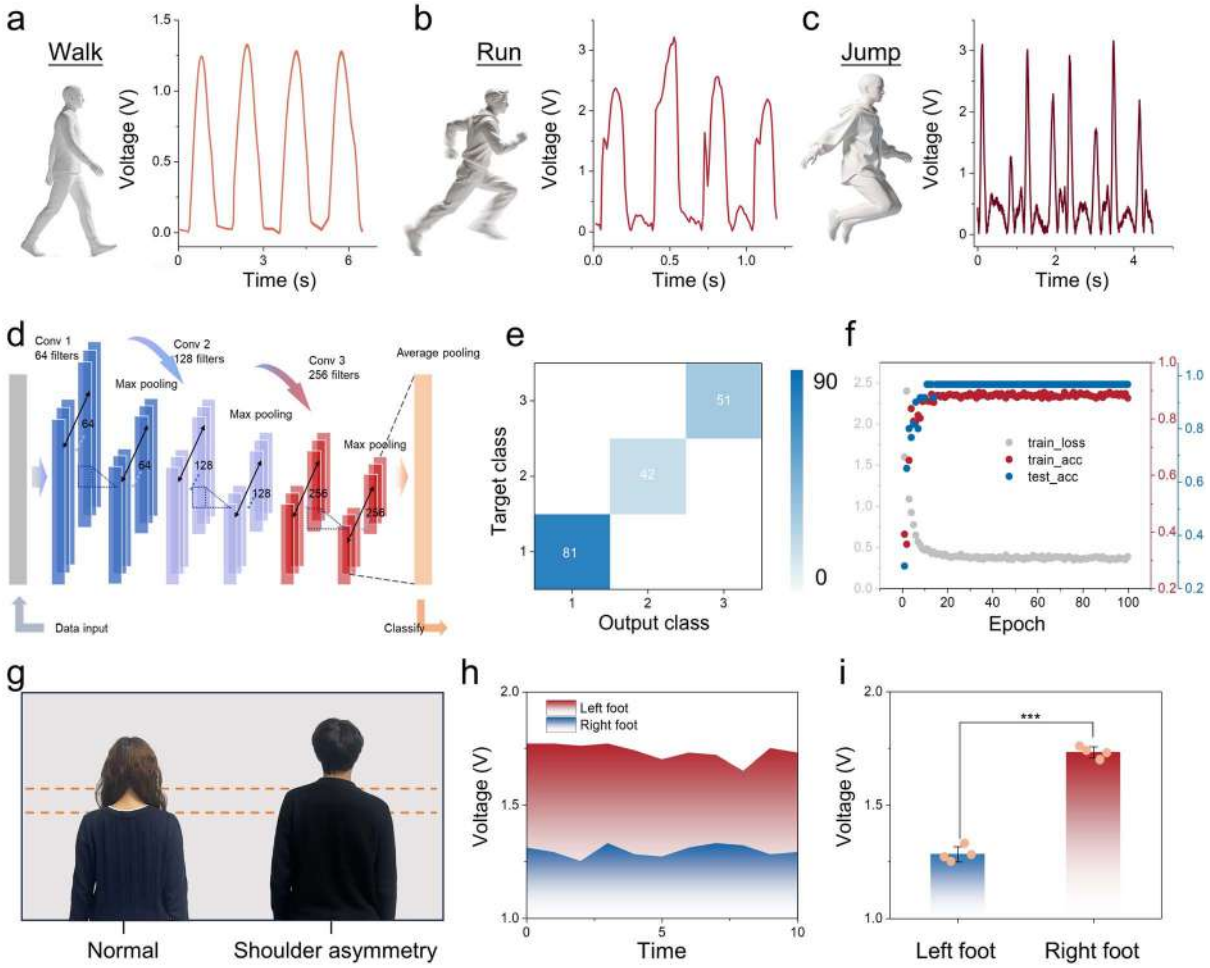


Fig. 4 Application of the sensor for human activity monitoring and recognizing. (a) Schematic diagram and corresponding signals of (a) walk, (b) run, and (c) jump. (d) Schematic diagram of constructed 1D-CNN model. (e) Confusion matrix for three kinds of activities. (f) Evaluation of classification, train accuracy and loss function in 100 epochs for five finger flexion. (g) Photographs comparing a normal shoulder and an asymmetric shoulder. (h) Piezoelectric signals recorded from the plantar surfaces of both feet in an individual with shoulder asymmetry. (i) Significant differences in piezoelectric signals acquired from the left and right feet.

(Fig. 4g), resulting in asymmetric plantar pressure signals. As illustrated in Fig. 4h, the temporal output signals from sensors placed on the left and right foot soles exhibited pronounced asymmetry in individuals with shoulder asymmetry compared with those with normal posture. Statistical analysis revealed a significant difference between the two signal groups (Fig. 4i and S13). These preliminary observations suggest that the sensor holds promise for detecting subtle postural abnormalities and early diagnosis.

Conclusions

In summary, an MMT/PT composite piezoelectric mat was designed to harness interfacial polarization for enhanced piezoelectric performance and applications in activity monitoring and intelligent healthcare. Structural and computational analyses confirmed that the interfacial polarization originates primarily from permittivity mismatch between the MMT nanosheets and the polymer matrix. Material characterization further demonstrated that this interfacial polarization promotes a *gauche* to all-*trans* conformational transition in the PT molecular chains. Electrical measurements revealed a concentration-dependent piezoelectric output, reaching a maximum at 4 wt% MMT—an eight-fold enhancement in voltage and a three-fold enhancement in current. The optimized sensor exhibited rapid response (30 ms) and recovery (60 ms) times, as well as operational stability over 5000 cycles under different conditions. When applied to monitor walking, running, and jumping, the sensor captured distinct motion signals and, in conjunction with a deep learning algorithm, achieved a classification accuracy of 96.7%. Moreover, by detecting plantar pressure asymmetry in individuals with shoulder asymmetry, the sensor demonstrated its potential for intelligent healthcare monitoring. This work establishes a valuable strategy for enhancing polymer piezoelectricity *via* low-*k* filler induced interfacial polarization and offers a promising material design platform for next-generation flexible wearable sensors.

 This journal is © The Royal Society of Chemistry 2026

Experimental section

Preparation of MMT/PT nanofiber mat

Preparation of MMT nanosheets. 0.5 g of montmorillonite (MMT, Sigma-Aldrich) was dispersed in 50 mL of *N*,*N*-dimethylacetamide (DMAc, Sigma-Aldrich) and subjected to ultrasonication for 4 hours. The resulting MMT/DMAc nanosheet suspension was collected by removing the sediment *via* centrifugation or sedimentation.

Preparation of MMT/PT nanofiber mat. 0.5 g $PT_{80:20}$ (Piezotech, Arkema) powder was added and dissolved in 5 mL *N*,*N*-dimethylacetamide (DMAc, Sigma-Aldrich) by stirring for 1 hour in a 40 °C water bath. The resulting MMT/DMAc suspension was then mixed with the PT solution. The composite mixture was loaded into a syringe for electrospinning, which was performed at a flow rate of 0.03 mL min^{-1} and a collector rotation speed of 1500 rpm. A high voltage of 12 kV was applied, with a working distance of 10 cm between the needle tip and the collecting roller. During the process, the temperature and humidity were maintained at 25 °C and 48%, respectively. The as-spun MMT/PT nanofiber mat was collected on an aluminum foil-covered collector and subsequently annealed at 60 °C for 2 hours.

Fabrication of piezoelectric sensors. The mats were cut into square (16 mm in diameter) using a laser cutter. Silver electrodes were then deposited onto both sides of the MMT/PT composite mat *via* magnetron sputtering under an argon atmosphere. The resulting piezoelectric sensor was subsequently encapsulated with polyurethane (PU) medical tape to ensure robust packaging.

Characterization

Material characterization. The morphology and composition of the materials were examined by field-emission scanning electron microscopy (FESEM; JSM 7800F, JEOL) and transmission electron microscopy (TEM; JEM 2100F, JEOL). The crystalline phase and structure were analyzed using X-ray diffraction (XRD; Empyrean, PANalytical) and Fourier-transform infrared spectroscopy (FTIR; Nicolet iS50, Thermo Fisher). Thermal properties were investigated by differential scanning calorimetry (DSC; DSC 2500, TA Instruments) over a temperature range from room temperature to 200 °C at a heating rate of 10 °C min^{-1}. Mechanical properties of the mats were evaluated using a universal tensile tester (LDW-1, Songdu Instrument) at a crosshead speed of 10 mm min^{-1}. The molecular orientation within the mats was assessed by small-angle X-ray scattering (SAXS; Xeuss 2.0, Xenocs). Finite element analysis (FEA) was conducted using COMSOL Multiphysics software.

Electric performance measurement. The electric performance of piezoelectric mats was characterized by a programmable electrometer (Keithley 6517). The periodic pressure was supplied by linear motor (LinMotH01-23 × 86/160) and was monitored by a force gauge (IMADA model ZPS-DPU-50N).

Deep learning for motion signal. The one-dimensional convolutional neural network (1D-CNN) was implemented with three convolutional layers for feature extraction and subsequent signal classification. For each type of input signal, ten independent measurements were recorded, each containing 1000 data points. The resulting dataset was randomly partitioned into training, validation, and test sets in an 8 : 1 : 1 ratio. The network was trained for 100 epochs to perform signal recognition, and the evolution of classification accuracy, training accuracy, and training loss was monitored to evaluate the deep learning performance.

Ethical statement

The sensors were attached to the skin surface of the participants for non-invasive signal acquisition. All participants were members of our research group and signed informed consent was obtained from them prior to the experiments.

Conflicts of interest

The authors declare no competing financial interest. They have no known competing financial interests or personal relationships that could have appeared to influence the work reported in this paper.

Data availability

All data generated or analyzed during this study are included in this published article (and its supplementary information (SI) files); all data are available from the corresponding author on reasonable request. Supplementary information is available. See DOI: https://doi.org/10.1039/d6ta05902c.

Acknowledgements

This research is supported by the National Natural Science Foundation of China (No. 52303328), the Postdoctoral Innovation Talents Support Program (No. BX20220257), the Doctoral Innovation Fund Program of Southwest Jiaotong University (No. CX2026YB13). Thanks for the help from the Analysis and Testing Center of Southwest Jiaotong University.

References

1 D. Won, J. Bang, S. H. Choi, K. R. Pyun, S. Jeong, Y. Lee and S. H. Ko, *Chem. Rev.*, 2023, **123**, 9982–10078.
2 X. Qian, X. Chen, L. Zhu and Q. M. Zhang, *Science*, 2023, **380**, eadg0902.
3 M. Guo, C. Guo, J. Han, S. Chen, S. He, T. Tang, Q. Li, J. Strzalka, J. Ma, D. Yi, K. Wang, B. Xu, P. Gao, H. Huang, L. Q. Chen, S. Zhang, Y. H. Lin, C. W. Nan and Y. Shen, *Science*, 2021, **371**, 1050–1056.
4 L. Gao, B.-L. Hu, L. Wang, J. Cao, R. He, F. Zhang, Z. Wang, W. Xue, H. Yang and R.-W. Li, *Science*, 2023, **381**, 540–544.
5 Z. Yuan, H. Tong, Z. Fei, C. Li and Y. Liu, *Nat. Commun.*, 2025, **16**, 8758.
6 Z. Gao, Y. Lei, Z. Li, J. Yang, B. Yu, X. Yuan, Z. Hou, J. Hong and S. Dong, *Prog. Mater. Sci.*, 2025, **151**, 101434.
7 C. M. Costa, V. F. Cardoso, P. Martins, D. M. Correia, R. Gonçalves, P. Costa, V. Correia, C. Ribeiro,

M. M. Fernandes, P. M. Martins and S. Lanceros-Méndez, *Chem. Rev.*, 2023, **123**, 11392–11487.
8 B. Lan, W. Deng, Y. Ao, Y. Sun, G. Tian, T. Yang, S. Wang, L. Huang, T. Zhou, P. Li, Z. Wang, T. Xu, G. Liu, J. Sun, H. Li, L. Jin, B. Zhang, F. Chun and W. Yang, *Nano Energy*, 2026, **156**, 112122.
9 G. Tian, W. Deng, T. Yang, J. Zhang, T. Xu, D. Xiong, B. Lan, S. Wang, Y. Sun, Y. Ao, L. Huang, Y. Liu, X. Li, L. Jin and W. Yang, *Adv. Mater.*, 2024, **36**, 2313612.
10 Y. Ao, L. Jin, S. Wang, B. Lan, G. Tian, T. Xu, L. Huang, Z. Wang, Y. Sun, T. Yang, W. Deng, F. Yang and W. Yang, *Nano-Micro Lett.*, 2025, **17**, 320.
11 W. Deng, Y. Zhou, A. Libanori, G. Chen, W. Yang and J. Chen, *Chem. Soc. Rev.*, 2022, **51**, 3380–3435.
12 J. Xue, T. Wu, Y. Dai and Y. Xia, *Chem. Rev.*, 2019, **119**, 5298–5415.
13 G. Yang, X. Li, Y. He, J. Ma, G. Ni and S. Zhou, *Prog. Polym. Sci.*, 2018, **81**, 80–113.
14 T. Tang, Z. Shen, J. Wang, S. Xu, J. Jiang, J. Chang, M. Guo, Y. Fan, Y. Xiao, Z. Dong, H. Huang, X. Li, Y. Zhang, D. Wang, L.-Q. Chen, K. Wang, S. Zhang, C.-W. Nan and Y. Shen, *Natl. Sci. Rev.*, 2023, **10**, nwad177.
15 D. Han, F. Du, Y. Zhang, L. Zheng, J. Chen, X. Huang, Q. Li, S. Zheng, J. Shi, J. Chen, J. Dong and X. Qian, *Joule*, 2023, **7**, 2174–2190.
16 Y. Kwon, Y. Kim, H. Lee and M. Ha, *J. Korean Inst. Electr. Electron. Mater. Eng.*, 2025, **38**, 1–7.
17 M. S. Kwak, K.-W. Lim, H. Y. Lee, M. Peddigari, J. Jang, C. K. Jeong, J. Ryu, W.-H. Yoon, S. N. Yi and G.-T. Hwang, *Nanoscale*, 2021, **13**, 8418–8424.
18 Y. Su, W. Li, X. Cheng, Y. Zhou, S. Yang, X. Zhang, C. Chen, T. Yang, H. Pan, G. Xie, G. Chen, X. Zhao, X. Xiao, B. Li, H. Tai, Y. Jiang, L.-Q. Chen, F. Li and J. Chen, *Nat. Commun.*, 2022, **13**, 4867.
19 N. A. Shepelin, P. C. Sherrell, E. N. Skountzos, E. Goudeli, J. Zhang, V. C. Lussini, B. Imtiaz, K. A. S. Usman, G. W. Dicinoski, J. G. Shapter, J. M. Razal and A. V. Ellis, *Nat. Commun.*, 2021, **12**, 3171.
20 A. K. Katiyar, A. T. Hoang, D. Xu, J. Hong, B. J. Kim, S. Ji and J.-H. Ahn, *Chem. Rev.*, 2023, **124**, 318–419.
21 M. Li, Q. Fan, L. Gao, K. Liang and Q. Huang, *Adv. Mater.*, 2024, **36**, 2312918.
22 E. Pomerantseva, F. Bonaccorso, X. Feng, Y. Cui and Y. Gogotsi, *Science*, 2019, **366**, eaan8285.
23 X. Shen, Q. Zheng and J.-K. Kim, *Prog. Mater. Sci.*, 2021, **115**, 100708.
24 S. Wang, W. Deng, H. Huang, Z. Yan, Y. Wang, T. Zhou, Y. Ao, Z. Wang, J. Zhang, G. Tian, B. Lan, Y. Sun, T. Xu, T. Yang, L. Huang, L. Jin, J. Lu and W. Yang, *Nat. Commun.*, 2026, **17**, 2471.
25 J. Yang, J. Wang, Z. Guo, S. Liu, Y. Dong, P. Zhou, T. Zhang and Y. Qi, *J. Alloys Compd.*, 2026, **1079**, 189867.
26 F. Mokhtari, A. Volodine, O. Deschaume, C. Bartic, A. de Kogel, X. Wang and R. J. Varley, *Energy Environ. Mater.*, 2026, e70348, DOI: 10.1002/eem2.70348.
27 Y.-J. Wu, J.-X. Guo, X. Zhao, C.-Y. Tang, T. Gong, Q. Jing, K. Ke, Y. Wang, R.-Y. Bao, K. Zhang, M.-B. Yang and W. Yang, *Prog. Mater. Sci.*, 2025, **150**, 101422.
28 X. Li, S. He, Y. Jiang, J. Wang, Y. Yu, X. Liu, F. Zhu, Y. Xie, Y. Li, C. Ma, Z. Shen, B. Li, Y. Shen, X. Zhang, S. Zhang and C.-W. Nan, *Nat. Commun.*, 2023, **14**, 5707.
29 B. Li, C. Cai, Y. Liu, F. Wang, B. Yang, Q. Li, P. Zhang, B. Deng, P. Hou and W. Liu, *Nat. Commun.*, 2023, **14**, 4000.
30 S. Zheng, F. Du, L. Zheng, D. Han, Q. Li, J. Shi, J. Chen, X. Shi, H. Huang, Y. Luo, Y. Yang, P. O'Reilly, L. Wei, N. de Souza, L. Hong and X. Qian, *Science*, 2023, **382**, 1020–1026.
31 S. Tu, Q. Jiang, X. Zhang and H. N. Alshareef, *ACS Nano*, 2018, **12**, 3369–3377.
32 F. Li, B. Wang, X. Gao, D. Damjanovic, L. Q. Chen and S. Zhang, *Science*, 2025, **389**, eadn4926.
33 Z. Zhu, G. Rui, E. Allahyarov, H. Zhang, R. Li, P. L. Taylor and L. Zhu, *Polymer*, 2025, **325**, 128290.
34 C. W. Nan, Y. Shen and J. Ma, *Annu. Rev. Mater. Res.*, 2010, **40**, 131–151.
35 X. Huang, B. Sun, Y. Zhu, S. Li and P. Jiang, *Prog. Mater. Sci.*, 2019, **100**, 187–225.
36 S. Wang, Z. Luo, J. Liang, J. Hu, N. Jiang, J. He and Q. Li, *ACS Nano*, 2022, **16**, 13612–13656.
37 A. A. Khan, A. Mathur, L. Yin, M. Almadhoun, J. Yin, M. H. Bagheri, M. F. A. Fattah, A. Rajabi-Abhari, N. Yan, B. Zhao, V. Maheshwari and D. Ban, *Nat. Commun.*, 2024, **15**, 9511.
38 G. Tian, W. Deng, D. Xiong, T. Yang, B. Zhang, X. Ren, B. Lan, S. Zhong, L. Jin, H. Zhang, L. Deng and W. Yang, *Cell Rep. Phys. Sci.*, 2022, **3**, 100814.

 This journal is © The Royal Society of Chemistry 2026